Surface and Defect Structure of Oxide Nanowires on $SrTiO_3$

Matthew S. J. Marshall,[1,*] Andres E. Becerra-Toledo,[2] Laurence D. Marks,[2] and Martin R. Castell[1,†]

[1]*Department of Materials, University of Oxford, Parks Road, Oxford, OX1 3PH, United Kingdom*

[2]*Department of Materials Science and Engineering, Northwestern University, Evanston Illinois 60208, USA*

(Received 28 January 2011; published 16 August 2011; corrected 8 September 2011)

Processing the $SrTiO_3(001)$ surface results in the self-assembly of reduced titanate nanowires whose widths are approximately 1 nm. We have imaged these nanowires and their defects at elevated temperatures by atomic resolution scanning tunneling microscopy. The nanowire structure is modeled with density functional theory, and defects observed in the center of the nanowire are determined to be Ti_4O_3 vacancy clusters. The activation energy for Ti_4O_3 vacancy cluster diffusion is explicitly measured as 4.98 ± 0.17 eV with an exponential prefactor of $\mu = 6.57 \times 10^{29}$ s^{-1}.

DOI: 10.1103/PhysRevLett.107.086102 PACS numbers: 68.35.Dv, 68.35.Fx, 68.47.Gh, 68.65.−k

The perovskite oxide $SrTiO_3$ has critical materials properties [1–4] that are being exploited in an emerging generation of nanoscale electronic devices [5,6]. Interest in $SrTiO_3$ has grown as a result of the discoveries that tailoring defect composition can drastically increase the electron mobility [7], and that it forms a 2D electron gas at the bare surface [8,9]. It is also a suitable substrate for the growth of high T_c superconductors [10] and epitaxial islands of anatase [11]. These developments revolve around tuning the defect structure in the near-surface and interface regions to achieve the desired electronic and optical properties. In parallel with these advances, structural solutions of the many surface reconstructions of $SrTiO_3$ have recently been achieved [12–14] and nonperovskite surface phases have been observed [15–17].

It is against this background of a rapidly increasing understanding of the atomic structure and optoelectronic properties of $SrTiO_3$ that we present the structural solution of linear titanate nanowires that spontaneously self-assemble on the $SrTiO_3(001)$ surface. We have also identified a typical nanowire defect, and determined its structure. In addition, we have used elevated temperature STM to measure the activation energy of the defect for diffusion. STM has been successfully used to study defect kinetics on some oxide surfaces, including vacancy and adatom diffusion [18–22], but to date defect diffusion in $SrTiO_3$ has been constrained to bulk studies [23–30]. Based on x-ray photoelectron spectroscopy (XPS), STM, and density functional theory (DFT) modeling, we propose a three layer ridge-and-valley type structure for the nanowire that includes a linear backbone containing reduced Ti. Furthermore, we propose that the typical defect in these nanowires is a Ti_4O_3 vacancy cluster, with a measured activation energy for diffusion of 4.98 ± 0.17 eV.

Three different types of linear nanostructures form on the surface of $SrTiO_3(001)$ after UHV annealing of an argon-ion sputtered surface: dilines, trilines, and tetralines [15]. All nanolines were shown to be stable in air and are unchanged when returned to UHV. The triline is thusly named since it consists of three parallel rows, oriented in the $\langle 001 \rangle$ directions. Figure 1(a) shows an STM image of a triline nanostructured surface of $SrTiO_3(001)$. Three other types of nanostructures termed metadilines, cross dots, and waffle structures can also be formed [15], several of which are visible in Fig. 1(a) adjacent to the trilines, but which play no role in this study. The triline surface exhibits (8×2) or (9×2) periodicity when found in close packed domains [15]. The outer two rows of the triline consist of bright spots separated by 0.78 nm, corresponding to twice the lattice constant of $SrTiO_3$ ($a_{SrTiO_3} = 0.3905$ nm). The backbone consists of bright spots separated by 0.39 nm. By changing the STM bias voltage, the ratio of backbone height to side row height is affected, indicating that the local density of states (LDOS) of the backbones differs from that of the surrounding surface [15].

Single crystal epipolished 0.5 wt % Nb-doped $SrTiO_3(001)$ (PI-KEM Ltd., U.K.) samples were used. Stoichiometric $SrTiO_3$ is insulating; thus, extrinsic n-type doping with Nb enables experimental analysis and preparation by rendering samples conductive. The samples were introduced into the ultrahigh vacuum (UHV) preparation chamber of a STM system (JEOL JSTM4500S) at a base pressure of 10^{-8} Pa. All sample preparation was carried out in the UHV-STM system in Oxford by Ar^+ sputtering with an energy of 1.0 kV for 10 min, followed by a 2 h anneal at 1173 K. This preparation protocol maximizes the coverage of triline nanostructures. X-ray photoelectron spectra of preprepared, air stable samples were obtained using a Scienta ESCA 300 spectrometer at the National Center for Electron Spectroscopy and Surface Analysis (NCESS) at the Daresbury Laboratory, U.K. Spectra were acquired using an Al $K\alpha$ source producing monochromatic radiation at an energy of 1486.7 eV with the incident beam at 45°. DFT was used to model structures using a repeated slab configuration of 11 atomic layers. All DFT calculations were carried out under the APW + lo implementation of the full-electron-potential WIEN2K code. Muffin-tin radii of 2.40, 1.68, and 1.50 Bohr were used for Sr, Ti,

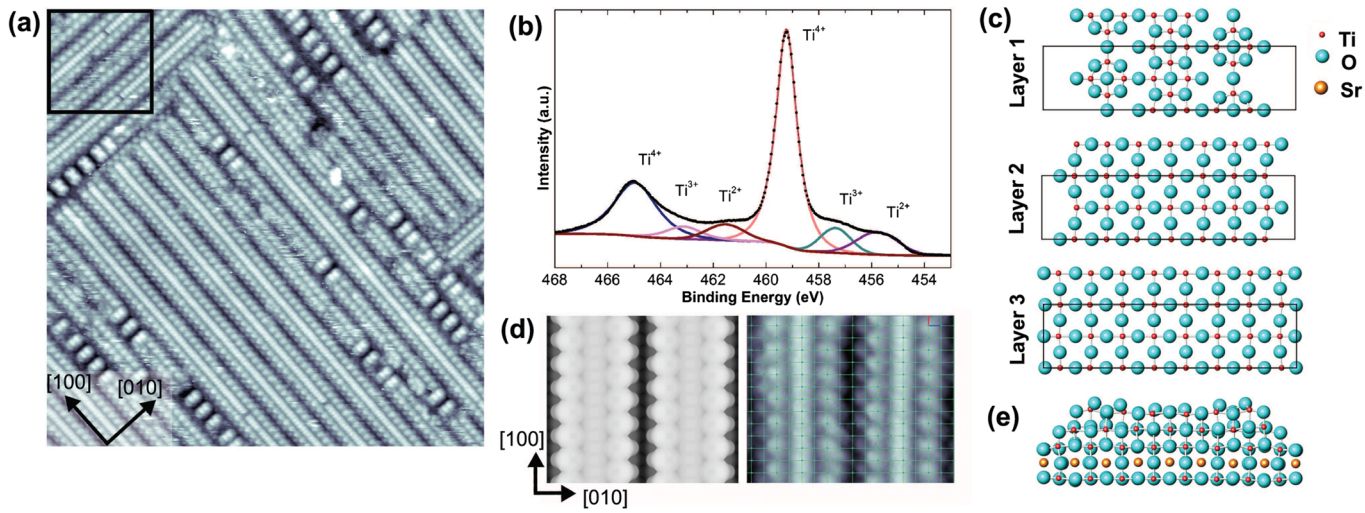

FIG. 1 (color online). An STM image of a triline nanostructured surface is shown in (a) with a field of view of 40×40 nm^2. The core level XPS Ti $2p$ spectrum shown in (b) is from a representative triline nanostructured surface showing the presence of a Ti^{2+} peak that arises exclusively from triline nanostructures and is attributed to the triline backbone. The Ti^{4+}, Ti^{3+}, and Ti^{2+} $2p_{1/2}$ peaks are shown at 465.0, 463.1, and 461.5 eV, respectively. The Ti^{4+}, Ti^{3+}, and Ti^{2+} $2p_{3/2}$ Ti peaks are shown at 459.2, 457.3, and 455.6 eV, respectively. The error associated with each XPS peak binding energy is ± 0.1 eV. In (c), the ball-and-stick structures are shown of the top three layers of a single triline nanostructure, modeled by DFT, are presented in plan view. The structures are shown with the side lobes in the ''zigzag'' or out-of-phase configuration. ''Layer 3'' sits atop a bulk SrO layer. An (8×2) unit cell is indicated. Simulated (6.2×5.5 nm^2) and experimental (6.8×5.5 nm^2) STM images of a triline nanostructure are shown in (d). A (1×1) mesh overlays the experimental STM image. The ball-and-stick structure of a single triline is shown in (e), presented in side view. The experimental STM imaging conditions are $V_s = +1.86$ V and $I_t = 0.24$ nA at $T = 791$ K.

and O atoms, respectively, along with a min(RMT) $* K_{\max}$ of 5.25. In each case, a k-point mesh equivalent to a $8 \times 8 \times 8$ mesh for a bulk $SrTiO_3$ unit cell was used. Each structure was allowed to relax such that all residual forces were below 0.2 eV/Å. The generalized gradient approximation (GGA), as defined by the PBE functional [31] was used as the exchange-correlation functional. Simulations of constant-current scanning tunneling microscopy (STM) images were generated using a version of the Tersoff and Hamann [32] theory, modified in order to capture high-bias effects [33], with the tip wave function expansion defined by Chen [34]. Using this formulation for the tunneling current, constant density surfaces were generated, thereby theoretically simulating STM images. In order to account for blurring due to nonzero tip size and thermal vibrations, the density array was convolved in-plane with a radially symmetric step-function feature. Since the PBE functional is known to underperform in strongly correlated systems, tests on preliminary structural models were performed with the PBE + U and hybrid PBE0 functionals. While there was a clear shift in the energies, no discernible difference was found in the simulations within the spatial resolution available in the experimental micrographs.

Figure 1(a) shows an STM image of a triline nanostructured surface. Some diline nanostructures and cross-dot nanostructures are also visible as is typical on these surfaces. Triline domains are approximately 15 nm wide, and 40 nm long, with a surface coverage of 50%. A high resolution core level XPS spectrum [Fig. 1(b)] of a representative triline nanostructured $SrTiO_3(001)$ surface shows the Ti $2p$ peaks. At the relevant photoelectron energies for Ti, the analysis depth is 1–1.5 nm. Ionization states are assigned to Ti peaks according to reference spectra, but more generally reflect the degree of surface titanium reduction. The large Ti^{4+} peak at 459.2 eV primarily corresponds to bulk TiO_2 layers, which would be expected from a fully stoichiometric surface. The presence of the Ti^{3+} peak at 457.3 eV can be attributed in part to structural aspects of the surface, but also arises as a result of reduction by Nb dopants, as well as O vacancies introduced during the sample preparation process. Approximately 8% of the total Ti peak area in Fig. 1(b) corresponds to Ti^{2+} at 455.6 eV. Unlike Ti^{3+}, the presence of Ti^{2+} can be unambiguously attributed to the structure of the top few monolayers. The Ti^{2+} peak is not present as a consequence of Nb doping, sputtering, or annealing and indeed is not visible on spectra of other surfaces decorated with similar linear nanostructures such as dilines and tetralines, or other nanostructures present on this surface such as cross dots. We can therefore conclude that the Ti^{2+} peak is entirely due to a structural feature of the trilines, rather than a result of valence charge compensation induced by defects and dopants.

The ball-and-stick model of the triline structure, modeled by DFT with an 8×2 supercell [Fig. 1(c)], exhibits a ridge-and-valley structure composed of three titanate

layers. A cif file of the full structure can be found at Ref. [35]. The topmost layer 1 is a reduced linear structure with a central backbone of Ti_3O_5 stoichiometry and side rows that consist of groups of four Ti atoms and seven oxygens linked to each other with oxygen atoms. These units are similar to the top layer of the $c(4 \times 2)$ reconstruction [36]. The second layer below has TiO_2 stoichiometry and sits atop a distorted layer of bulk TiO_2, below which there is a bulk SrO layer. Simulated STM images of two adjacent trilines are compared to experimental STM images in Fig. 1(d), where the $c(4 \times 2)$ units appear as single round spots. This is in good agreement with the adjacent STM images that also show single large spots. Additionally, this simulation reconciles a long-standing difference in the appearance of the $c(4 \times 2)$ surface in STM images [37] with the structure determined by Erdman *et al.* [36]. The heavily reduced backbone of the triline gives rise to the Ti^{2+} peak in the XPS spectrum in Fig. 1(b). Each bright spot along the length of the triline backbone corresponds to a linear unit of Ti_2O_3. In this configuration, all Ti atoms lie on top of O atoms and vice versa, except for the central-row O atoms, which have no cations sitting immediately underneath them. This registry with the bulk was calculated to be energetically much more stable than other alternatives.

Figure 2 compares STM images of two defects in the triline backbone to simulated images of such defects, modeled in DFT with one defect per 8×4 supercell. A cif file of the full structure can be found at Ref. [38]. A Ti_4O_3 vacancy along the backbone of the triline manifests itself in STM images and simulations as a dark spot on the triline backbone. Several such vacancy clusters are visible in [Fig. 1(a)] as dark spots along the backbones of the trilines. The defect in Fig. 2 was therefore determined

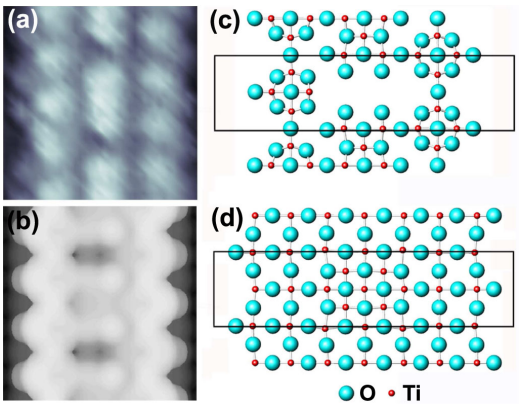

FIG. 2 (color online). (a) Two Ti_4O_3 vacancy cluster defects are shown in experimental STM and (b) simulated STM images (3.12×3.12 nm^2 each). The ball-and-stick structure of the topmost layer of the defect is shown in (c). In (d), the four Ti atoms from the top layer are found to reside in the second layer. The STM imaging conditions are $V_s = +1.86$ V and $I_t = 0.24$ nA at $T = 791$ K.

to be a Ti_4O_3 vacancy cluster, which produced good agreement between the experimental and simulated STM images. While many different defect configurations were explored, only the Ti_4O_3 configuration was found to be structurally and energetically realistic. A ball-and-stick model of the top layer of the defect structure is shown in Fig. 2(c), in which a linear O-Ti-O-Ti-O unit is missing, as well as two Ti atoms adjacent to the central missing oxygen. The four Ti atoms from the top layer are now found to reside in the second layer of the structure. Simulations of cases where there is no Ti in the second layer show elevated second layer oxygens and exhibit a poor match with experimental STM images. Removing a Ti_4O_3 unit from the triline backbone does not affect the appearance of the rest of the triline in STM simulations, in agreement with experimental STM images, as shown in Fig. 2.

A close-up of the inset area of Fig. 1(a) is shown [Fig. 3(a)] where two Ti_4O_3 vacancy clusters are indicated by black arrows. Sequential imaging in the UHV-STM at elevated temperatures allows for observation of the vacancy cluster diffusion process. In Figs. 3(a)–3(d) the positions of the black arrows are affixed to the starting locations of two vacancy clusters. These two defects can be observed hopping back and forth along the backbones of the trilines. There were no observed instances of vacancy clusters diffusing from the backbone to the outer two rows. A movie of the vacancy cluster diffusion is located at Ref. [39], as well as a digital zoom of the area of interest shown in Ref. [40].

Figure 3(e) shows a plot of the vacancy cluster hopping rates versus temperature. The defect hopping rate was determined by measuring the average displacement of the defect in two STM images taken 90 sec apart [21]. The data have been fitted to the Arrhenius diffusion equation, $h = \nu \exp(-E_a/k_B T)$, where h is the hopping rate, E_a is the diffusion activation energy, k_B is Boltzmann's constant, and T is the temperature. The kinetic parameters E_a and ν can then be extracted, yielding an experimentally determined activation energy for Ti_4O_3 vacancy cluster diffusion of $E_a = 4.98 \pm 0.17$ eV, with an exponential prefactor of $\nu = 6.57 \times 10^{29}$ s^{-1}. This activation energy is for vacancy clusters that were not observed to interact with other defects, or with the end of a triline. Also, there is no evidence of burst hopping, which is the hopping back and forth that would indicate diffusion mediated by subsurface defects [41]. The high activation energy measured here is appropriate given the size of the vacancy cluster.

Our results indicate that the backbones of the triline nanostructures on the surface of $SrTiO_3$ consist of O and reduced Ti. Using a combination of techniques we have solved the structure of the triline nanowire, which exhibits excellent agreement between experimental STM images and simulations. Furthermore, we have solved the structure of a vacancy cluster of Ti_4O_3 on a perovskite oxide, and measured the activation energy for the 1D diffusion of a

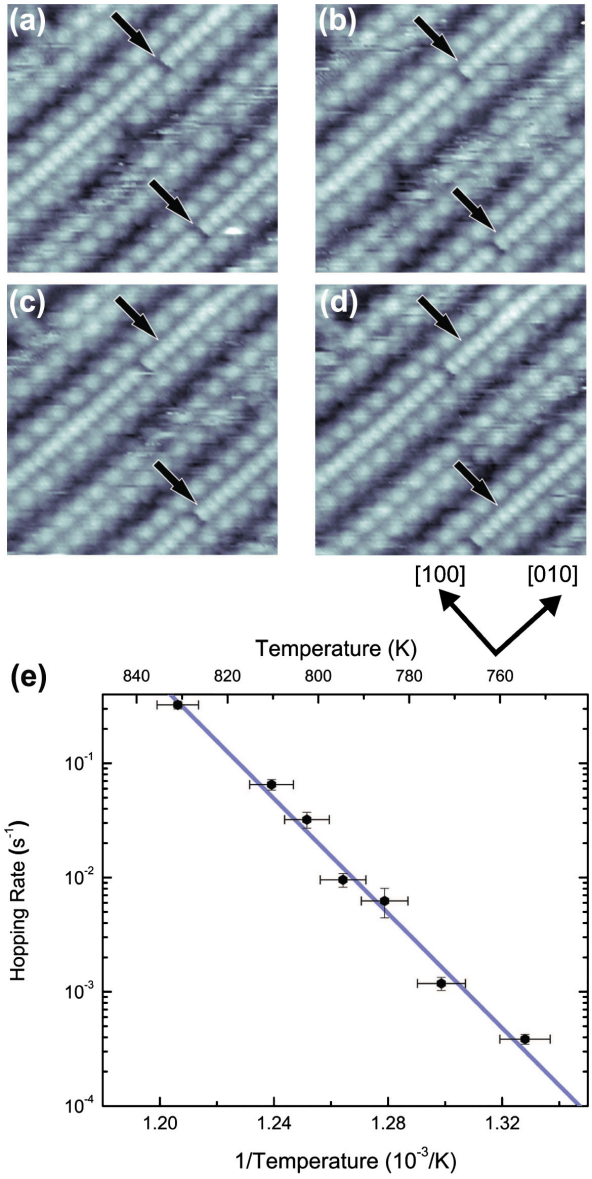

FIG. 3 (color online). (a)–(d) Sequential STM images ($\Delta t = 90$ sec) that are close-ups of the inset area of Fig. 1(a), and are also shown in the STM movie [39]. The field of view is 9.5×9.5 nm^2. The arrows in (a)–(d) locate the starting positions of the indicated vacancies at $t = 0$ sec. The images were obtained at a constant temperature, $T = 791$ K, and imaging conditions as $V_s = +1.86$ V and $I_t = 0.24$ nA. (e) Arrhenius diffusion plot of the hopping rates h at seven different temperatures ranging from 753–829 K. Each point corresponds to 50–75 observed hopping events.

Ti_4O_3 vacancy cluster along the length of the backbone to be 4.98 ± 0.17 eV. This work addresses the structure of vacancy clusters and solves the structure of the previously observed triline nanowires. The results in this Letter greatly enhance our understanding of the physical structure of oxide nanowires, and provide a route for discovery of similar nonperovskite nanostructured surfaces on other technologically relevant oxides.

The authors would like to thank Chris Spencer (JEOL U.K.) for technical assistance and JEOL U.K. for funding. L. D. M. and M. R. C. gratefully acknowledge the contribution from NSF/EPSRC Grant No. EP/F028784/1 for aiding this work. A. E. B. and L. D. M. acknowledge support by the National Science Foundation on Grant No. DMR 0906306.

*Present Address: CRISP, Department of Applied Physics, Yale University, New Haven, CT, USA.
†martin.castell@materials.ox.ac.uk

[1] C. H. Ahn, K. M. Rabe, and J. M. Triscone, Science **303**, 488 (2004).
[2] D. W. Reagor and V. Y. Butko, Nature Mater. **4**, 593 (2005).
[3] H. Ohta *et al.*, Nature Mater. **6**, 129 (2007).
[4] A. Ohtomo and H. Y. Hwang, Nature (London) **427**, 423 (2004).
[5] K. Szot *et al.*, Nature Mater. **5**, 312 (2006).
[6] C. Cen *et al.*, Science **323**, 1026 (2009).
[7] Y. Kozuka, Y. Hikita, C. Bell, and H. Y. Hwang, Appl. Phys. Lett. **97**, 012107 (2010).
[8] A. F. Santander-Syro *et al.*, Nature (London) **469**, 189 (2011).
[9] W. Meevasana *et al.*, Nature Mater. **10**, 114 (2011).
[10] C. H. Ahn *et al.*, Science **284**, 1152 (1999).
[11] M. S. J. Marshall and M. R. Castell, Phys. Rev. Lett. **102**, 146102 (2009).
[12] N. Erdman *et al.*, Nature (London) **419**, 55 (2002).
[13] J. A. Enterkin *et al.*, Nature Mater. **9**, 245 (2010).
[14] R. Herger *et al.*, Phys. Rev. Lett. **98**, 076102 (2007).
[15] D. S. Deak, F. Silly, D. T. Newell, and M. R. Castell, J. Phys. Chem. B **110**, 9246 (2006).
[16] H. L. Marsh, D. S. Deak, F. Silly, A. I. Kirkland, and M. R. Castell, Nanotechnology **17**, 3543 (2006).
[17] M. R. Castell, Surf. Sci. **516**, 33 (2002).
[18] R. Otero *et al.*, Nature Mater. **3**, 779 (2004).
[19] F. Besenbacher, E. Lægsgaard, and I. Stensgaard, Mater. Today **8**, 26 (2005).
[20] S. Wendt *et al.*, Phys. Rev. Lett. **96**, 66107 (2006).
[21] Z. Zhang *et al.*, Phys. Rev. Lett. **99**, 126105 (2007).
[22] Z. Zhang *et al.*, Phys. Rev. Lett. **101**, 156103 (2008).
[23] K. Gömann *et al.*, Phys. Chem. Chem. Phys. **6**, 3639 (2004).
[24] A. E. Paladino, L. G. Rubin, and J. S. Waugh, J. Phys. Chem. Solids **26**, 391 (1965).
[25] W. H. Rhodes and W. H. Kingery, J. Am. Ceram. Soc. **49**, 521 (1966).
[26] M. J. Akhtar *et al.*, J. Am. Ceram. Soc. **78**, 421 (1995).
[27] D. D. Cuong *et al.*, Phys. Rev. Lett. **98**, 115503 (2007).
[28] M. Choi, F. Oba, and I. Tanaka, Phys. Rev. Lett. **103**, 185502 (2009).
[29] D. J. Keeble, S. Wicklein, R. Dittmann, L. Ravelli, R. A. Mackie, and W. Egger, Phys. Rev. Lett. **105**, 226102 (2010).
[30] D. J. Keeble, R. A. Mackie, W. Egger, B. Lowe, P. Pikart, C. Hugenschmidt, and T. J. Jackson, Phys. Rev. B **81**, 064102 (2010).

[31] J. P. Perdew, K. Burke, and M. Ernzerhof, Phys. Rev. Lett. **77**, 3865 (1996).
[32] J. Tersoff and D. R. Hamann, Phys. Rev. Lett. **50**, 1998 (1983).
[33] K. Stokbro, U. Quaade, and F. Grey, Appl. Phys. A **66**, S907 (1998).
[34] C. J. Chen, *Introduction to Scanning Tunneling Microscopy* (Oxford University Press, New York, 1993).
[35] See Supplemental Material at http://link.aps.org/supplemental/10.1103/PhysRevLett.107.086102 for the cif file of the triline structure shown in Fig. 1.
[36] N. Erdman *et al.*, J. Am. Chem. Soc. **125**, 10050 (2003).
[37] M. R. Castell, Surf. Sci. **505**, 1 (2002).
[38] See Supplemental Material at http://link.aps.org/supplemental/10.1103/PhysRevLett.107.086102 for the cif file of the triline nanostructure containing a Ti_4O_3 vacancy cluster.
[39] See Supplemental Material at http://link.aps.org/supplemental/10.1103/PhysRevLett.107.086102 for the STM movie of a Ti_4O_3 defect diffusing along the length of a triline nanostructure, shown in Fig. 3 at a larger scale.
[40] See Supplemental Material at http://link.aps.org/supplemental/10.1103/PhysRevLett.107.086102 for a digital zoom of the STM movie of a Ti_4O_3 defect diffusing along the length of a triline nanostructure, shown in Fig. 3.
[41] E. Bussmann *et al.*, Phys. Rev. Lett. **101**, 266101 (2008).